Green Synthesis of Biphasic TiO2-Reduced Graphene Oxide Nanocomposites With Highly Enhanced Photocatalytic Activity

5 AUTHORS, INCLUDING:

Selim Sher shah
Sungkyunkwan University
16 PUBLICATIONS   **294** CITATIONS

SEE PROFILE

Zhang Kan
Sungkyunkwan University
22 PUBLICATIONS   **412** CITATIONS

SEE PROFILE

Jong Hyeok Park
Sungkyunkwan University
215 PUBLICATIONS   **5,336** CITATIONS

SEE PROFILE

Pil J. Yoo
Sungkyunkwan University (SKKU)
86 PUBLICATIONS   **3,068** CITATIONS

SEE PROFILE

Green Synthesis of Biphasic TiO$_2$–Reduced Graphene Oxide Nanocomposites with Highly Enhanced Photocatalytic Activity

Md. Selim Arif Sher Shah,[†] A Reum Park,[†] Kan Zhang,[‡] Jong Hyeok Park,[†,‡] and Pil J. Yoo[†,‡,*]

[†]School of Chemical Engineering and [‡]SKKU Advanced Institute of Nanotechnology (SAINT), Sungkyunkwan University, Suwon 440-746, Republic of Korea

S *Supporting Information*

ABSTRACT: A series of TiO$_2$–reduced graphene oxide (RGO) nanocomposites were prepared by simple one-step hydrothermal reactions using the titania precursor, TiCl$_4$ and graphene oxide (GO) without reducing agents. Hydrolysis of TiCl$_4$ and mild reduction of GO were simultaneously carried out under hydrothermal conditions. While conventional approaches mostly utilize multistep chemical methods wherein strong reducing agents, such as hydrazine, hydroquinone, and sodium borohydride are employed, our method provides the notable advantages of a single step reaction without employing toxic solvents or reducing agents, thereby providing a novel green synthetic route to produce the nanocomposites of RGO and TiO$_2$. The as-synthesized nanocomposites were characterized by several crystallographic, microscopic, and spectroscopic characterization methods, which enabled confirmation of the robustness of the suggested reaction scheme. Notably, X-ray diffraction and transmission electron micrograph proved that TiO$_2$ contained both anatase and rutile phases. In addition, the photocatalytic activities of the synthesized composites were measured for the degradation of rhodamine B dye. The catalyst also can degrade a colorless dye such as benzoic acid under visible light. The synthesized nanocomposites of biphasic TiO$_2$ with RGO showed enhanced catalytic activity compared to conventional TiO$_2$ photocatalyst, P25. The photocatalytic activity is strongly affected by the concentration of RGO in the nanocomposites, with the best photocatalytic activity observed for the composite of 2.0 wt % RGO. Since the synthesized biphasic TiO$_2$–RGO nanocomposites have been shown to effectively reduce the electron–hole recombination rate, it is anticipated that they will be utilized as anode materials in lithium ion batteries.

KEYWORDS: *titania, graphene, nanocomposites, green synthesis, hydrothermal, photocatalysis*
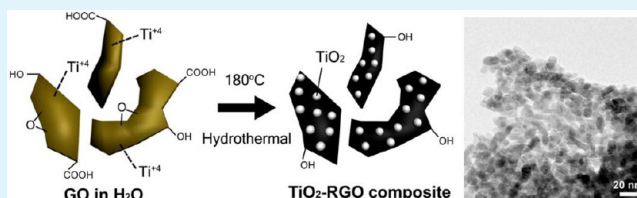
■ INTRODUCTION

Semiconductor nanocrystals have drawn great attention because of their outstanding physicochemical properties and strong potential for applications in energy conversion devices, supercapacitors, and photocatalysis.[1,2] Among them, TiO$_2$ has been considered as one of the most promising material because of its superior photocatalytic performance, easy availability, long-term stability, and nontoxicity.[3,4] Since the first demonstration of water splitting over TiO$_2$ by Fujishima and Honda in 1972, the photocatalytic properties of TiO$_2$ have been extensively studied.[5] However, the photocatalytic activity of TiO$_2$ is limited by its wide band gap energy (3.2 and 3.0 eV for anatase and rutile phase, respectively), which renders a limited capability of absorbing only the UV region of the solar spectrum. Under irradiation of solar light, electron–hole pairs that are responsible for its photocatalytic activity can be generated in TiO$_2$. However, the photogenerated electron–hole pairs have a flash recombination time on the order of 10^{-9} s, while the time scale of chemical interactions of TiO$_2$ with the adsorbed dye or chemicals is in the slower range of 10^{-8}–10^{-3} s.[6] This discrepancy between two time scales results in an unintended recombination of electron–hole pairs, leading to decreased efficiency in the photocatalytic activity of TiO$_2$. Therefore, besides its high band gap energy, another

challenging issue in the photocatalytic utilization of TiO$_2$ is overcoming the quick recombination of the photogenerated electrons and holes.

A number of strategies have been proposed to challenge these limitations. One important approach is to employ metal-ion or nonmetal doping to the crystalline TiO$_2$. This strategy can decrease the electron–hole pair recombination rate, which substantially enhances the interfacial charge-transfer reaction rate.[7−9] However, the synthesized materials typically suffer from a low concentration of doped ions and/or show low stability against photocorrosion.[10,11] Synthesis of TiO$_2$–based composites via the incorporation of noble metal nanoparticles is known to enhance the photocatalytic performance, since noble metals can lock the photogenerated electrons. Subsequently, the electron transfer rate at the interface increases, which leads to an increase in the photocatalytic activity of TiO$_2$.[12,13] Another popular means is to make composites of TiO$_2$ with other metal oxides, such as SnO$_2$, MoO$_3$, WO$_3$, and Fe$_2$O$_3$.[14−17] However, this strategy has the shortcoming of multistep reaction pathways. Moreover, the composite system
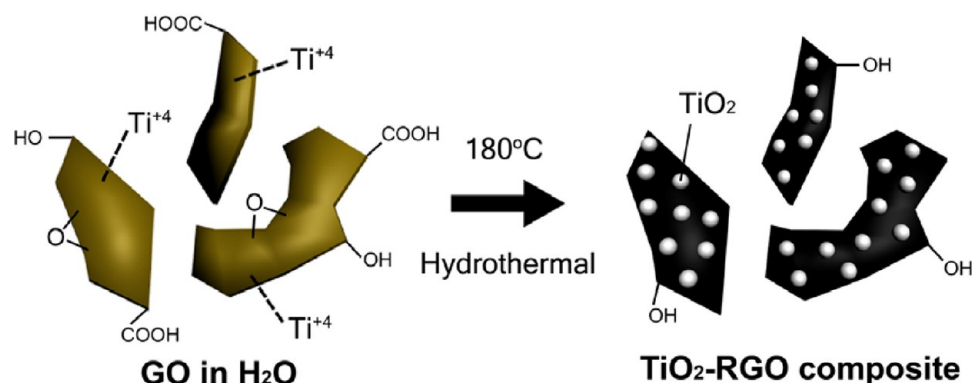
Figure 1. Reaction scheme of synthesizing TiO_2−reduced graphene oxide nanocomposites.

often leads to a decrease in the photocatalytic activity due to the partial loss of active surface sites of the photocatalyst.[18]

As an innovative new material, graphene has recently been shown to exhibit many extraordinary physical properties, such as high chemical stability, notably high specific surface area ($\sim$2600 m^2 g^{-1}), excellent mobility of charge carriers (20,000 cm^2 V^{-1} s^{-1}) and relatively good optical transparency.[19−21] On the basis of this understanding, composites of graphene and TiO_2 have shown advantageous enhancement of photocatalytic activity in a number of studies because the graphene can facilitate charge separation and do a function when used as an electron carrier in composite materials.[22−25] Several synthetic techniques such as chemical reduction using hydrazine, UV-assisted photoreduction, sol−gel method, atomic layer deposition (ALD), or solvothermal method have been employed for the preparation of TiO_2−graphene composites.[26−29] Notably, in most reported methods, the P25 nanoparticles was used as a counter-component to the graphene in the composites.[22,23,30] However, this tactic severely limits the tunability of the composite properties since one species is already fixed in the binary composites. In other cases, titanium alkoxides are widely employed as a TiO_2 precursor.[31] Owing to the high reactivity of alkoxides, however, sophisticate control over reaction conditions is essential during solution-based synthesis.[32]

Herein, we report a facile and robust one-step synthesis of TiO_2−graphene composite and its performance in photocatalytic applications. The most notable aspect of our approach is the use of an aqueous solution and lack of harsh chemicals (such as hydrazine) during synthesis. The reduction of graphite oxide, hydrolysis of $TiCl_4$, and the crystallization of the produced TiO_2 are concurrently carried out in a single-step reaction by hydrothermal treatment. We therefore effectively exclude the use of titanium alkoxides as highly reactive reagent or hydrazine as a toxic reducing agent, which have been encountered in synthetic conditions in conventional systems.[33,34] Accordingly, the proposed approach is highly energy-efficient and environmentally benign, making it truly green. In addition, in the synthesized catalysts, TiO_2 is present in both anatase and rutile phases, whereas the reported methods have mainly dealt with a single phase.[22−26] The catalysts show enhanced photocatalytic activity toward the degradation of the rhodamine B dye and benzoic acid under visible light irradiation.

■ EXPERIMENTAL SECTION

Materials. Graphite powder (<20 μm, synthetic) and titanium tetrachloride ($TiCl_4$) were purchased from Sigma-Aldrich. $NaNO_3$ (99.0%) was obtained from Yakuri Pure Chemicals Co. Ltd. Japan. H_2SO_4 (95.0%), $KMnO_4$ (99.3%), and H_2O_2 (34.5%) were purchased from Samchun Chemical Co. Ltd., Korea. The commercial P25 TiO_2 supplied by Degussa Corporation was used for comparison. All the chemicals were used as received and without further purification. In all experiments deionized water of resistance 18.2 MΩ was used.

Synthesis of Graphene Oxide. Graphene oxide (GO) was prepared from graphite powder using a modified Hummer's method.[35,36] In brief, first, 0.5 g of powdered flake of graphite and 0.5 g of $NaNO_3$ were added into 24 mL of H_2SO_4 and were stirred until dissolved. Then, 3 g of $KMnO_4$ was added slowly, preventing the temperature of the suspension from exceeding 20 °C. After the mixture was stirred continuously for 1 h at 35 °C, 40 mL of distilled water was slowly added to dilute the mixture and the temperature was raised to 90 °C. To reduce the residual permanganate and manganese dioxide to colorless soluble manganese sulfate, 5 mL of 34.5% H_2O_2 was added and the suspension was filtered with distilled water until pH 7.0. The obtained yellow-brown suspension was exfoliated to produce single layer graphene oxide using a sonicator, and the unexfoliated precipitation was removed by centrifugation. Finally, we obtained a brown dispersion of homogeneously exfoliated graphene oxide.

Synthesis of Titania-Reduced Graphene Oxide (RGO) Composites. The synthesis of titania−RGO composites is shown in Figure 1. In a typical reaction, the water dispersion of graphene oxide was sonicated for 15 min under cold conditions. The resulting dispersion was centrifuged at 6000 rpm for 5 min and the supernatant was collected and kept in a refrigerator. Then, 0.2 mL of $TiCl_4$ was added to the 31.0 mL of ice-cooled solution under vigorous stirring. After stirring for 1.5 h at room temperature the brown solution (total volume 31.2 mL) was transferred to a 50 mL Teflon lined stainless steel autoclave for hydrothermal reaction at 180 °C for 8 h. The autoclave was cooled naturally. The resulting black product, was collected by centrifugation and washed with deionized water and ethanol. It was then dried at 60 °C. In this way, nanocomposites of graphene and titania were synthesized where both anatase and rutile phases of titania were present. Meanwhile, individual titania and RGO for control were synthesized separately following the same procedure.

Photocatalytic Experiment. The photocatalytic activity of the as-prepared catalysts was measured by the photodegradation of a rhodamine B (RhB) solution under the illumination of visible light at ambient temperature. In a typical reaction, 30 mg of the catalyst was dispersed in 50 mL of a 2 × 10^{-5} M RhB solution under ultrasonication for 1 min. Before illumination, the mixture was magnetically stirred for 1 h in the dark to establish adsorption−desorption equilibrium of the dye with the catalyst. A solar simulator with Xe lamp (LS-150-Xe, Abet Technologies, Inc., USA) was used as the visible light source. The experimental solution was placed in a quartz cuvette and placed at a distance of 100 mm from the light source. At given intervals, 3 mL of the suspension was withdrawn and

centrifuged to remove the dispersed catalyst powder. The concentration of the clean transparent solution was determined by measuring the absorbance of RhB at 553 nm using a spectrophotometer (UV-3600, Shimadzu, Japan). A benzoic acid (BA, Sigma Aldrich) degradation experiment was also carried out following the same procedure, except, the initial concentration of BA was 1.31×10^{-4} M and it was stirred with the catalyst of TiO_2−5 wt % RGO in the dark for 2 h.

Characterization. Powder X-ray diffraction (XRD) patterns were obtained (D8 Focus, Bruker instrument, Germany) with Cu Kα radiation ($\lambda = 1.5406$ Å) in the 2θ range from 3 to 80° with a step size of 0.02° s^{-1}. The accelerating voltage and the applied current were 40 kV and 40 mA, respectively. Transmission electron microscopy (TEM, JEM-3010, JEOL, Japan) was carried out with an acceleration voltage of 300 kV. FTIR measurements (IFS-66/S, Bruker instrument, Germany) were carried out in the transmittance mode in the spectral range 400−4000 cm^{-1} with a resolution better than 0.1 cm^{-1}. UV−visible absorption spectra were collected from the UV−vis−NIR spectrophotometer (UV-3600, Shimadzu, Japan). Raman spectra were taken using a Micro-Raman spectrometer system (ALPHA 300M, WITec, Germany). The sample was loaded on silica wafer and focused using a 50× objectives. The spectra were taken in the range 1−3000 cm^{-1}. The Brunauer−Emmett−Teller (BET) specific surface areas and porosity of the samples were evaluated on the basis of nitrogen adsorption isotherms measured at −196 °C using a gas adsorption apparatus (ASAP 2020, Micromeritics, USA). All the samples were degassed at 180 °C before nitrogen adsorption measurements. The BET surface area was determined using adsorption data in the relative pressure (p/p_0) range of 0.06−0.2. X-ray photoelectron spectroscopy (XPS) characterization was performed (ESCA 2000 instrument, VG Microtech, United Kingdom) with Al Kα X-ray source. All binding energy values were corrected by calibrating the C 1s peak at 284.6 eV. High resolution peaks were deconvoluted using Gaussian−Lorentzian functions with identical full width at half maxima (fwhm) after a Shirly background subtraction.

RESULTS AND DISCUSSION

In Figure 2, the XRD pattern of GO shows a major peak at $2\theta = 10.4°$, corresponding to a d-spacing of 0.95 nm, which is much
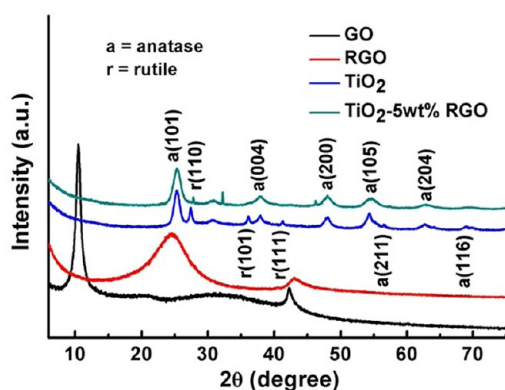

Figure 2. X-ray diffractograms of GO, RGO, TiO_2, and TiO_2−RGO.

larger than the d-spacing of natural graphite at 0.335 nm. This change indicates that graphite is oxidized to form GO.[37] After hydrothermal treatment, this peak disappears and a new peak centered at $2\theta = 24.5°$, corresponding to the d-spacing of graphene at 0.377 nm appears, indicating the reduction of GO to RGO.[38] As shown in the diffractogram, pure titania synthesized by the hydrothermal route shows good crystallinity. The peaks of 2θ values at 25.3, 37.9, 48.0, 54.4, 56.6, 62.8, and 68.9° can be indexed to (101), (004), (200), (105), (211), (204), and (116) planes of anatase titania, respectively.[39−41] On

the other hand, the characteristic diffraction peaks at 2θ values 27.4/27.8, 36.1, and 41.3 are assigned to (110), (101), and (111) crystal faces of rutile TiO_2.[40,41] The peaks corresponding to the anatase and rutile phases are denoted by "a" and "r", respectively. Therefore, it is clear from the XRD patterns that the nanocomposites have titania in both the anatase and the rutile phases, which is unique to our synthesized materials. Whereas, previously reported methods in which titania were synthesized (not P25) mostly dealt with a single phase of anatase. The relative composition of the anatase and rutile phase can be determined by comparing the intensities of the anatase (101), $A_{anatase}$ and rutile (110), A_{rutile} reflection planes by applying the following equation:[42]

$$x_{rutile} = \left(1 + \frac{A_{anatase}}{1.26 A_{rutile}} \right)^{-1} \tag{1}$$

Using eq 1, the content of rutile and anatase modifications in the synthesized materials are calculated as presented in Table 1.

Table 1. Estimated Relative Composition of Anatase and Rutile Phases in the Synthesized Materials

samples	anatase^a (%)	rutile (%)
P25	85.2	14.8
TiO2	65.8	34.2
TiO$_2$−1 wt % RGO	75.8	24.2
TiO$_2$−2 wt % RGO	75.5	24.5
TiO$_2$−5 wt % RGO	81.6	18.4
TiO$_2$−10 wt % RGO	87.9	12.1

^{a}Relative weight fraction.

The as-synthesized TiO_2−RGO nanocomposite shows a diffraction pattern similar to that of pure titania. It should be noted that there is no separate peak for RGO in the TiO_2−RGO composite, possibly due to the low amount and low intensity of RGO. Moreover, the characteristic peak of RGO at 24.5° may be screened by the main peak of anatase TiO_2 at 25.3°.[43] It is noticeable in Table 1 that the amount of anatase phase generally increases with an increase in the concentration of RGO, although there is no clear difference in the amount of this phase at a low amount of RGO. The same observation has been reported for the composites of TiO_2 and activated carbon.[44] It is attributed to the high surface area of graphene, which suppresses the phase transformation from anatase to rutile.

Morphological and structural features of the synthesized powders were examined by TEM. Figure 3A shows a TEM micrograph of RGO. Figure 3 panels B and C confirm that the TiO_2−RGO composites consist of large amounts of TiO_2 nanoparticles with sizes ranging from 12−16 nm. Notably, intraparticle aggregation forms a mesoporous structure, which is further confirmed by nitrogen adsorption−desorption analysis (details below). Figure 3D depicts a high resolution TEM (HRTEM) image of the TiO_2−RGO nanocomposites. The observed fringe spacings of 0.35 nm ensures the presence of anatase (101) planes, whereas the spacing of 0.32 nm indicates rutile (110) planes are present.[42]

Figure 4A shows Fourier transform infrared spectroscopy (FTIR) spectra of the synthesized TiO_2, RGO and TiO_2−RGO nanocomposite. The FTIR spectra of the synthesized TiO_2 show a broad band below 1000 cm^{-1}, which is attributed to the Ti−O−Ti stretching and bending vibrational modes. It also
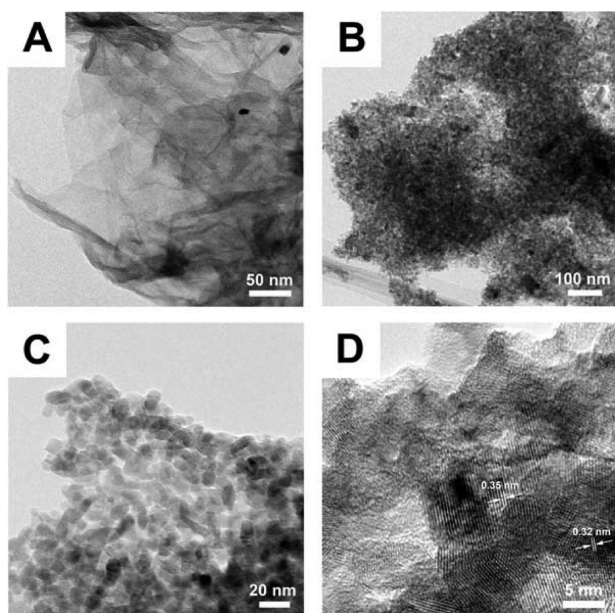
Figure 3. Typical TEM micrographs of (A) RGO, (B and C) TiO$_2$–RGO nanocomposites. (D) HRTEM image of TiO$_2$–RGO nanocomposites exhibiting mixed phases of anatase and rutile.
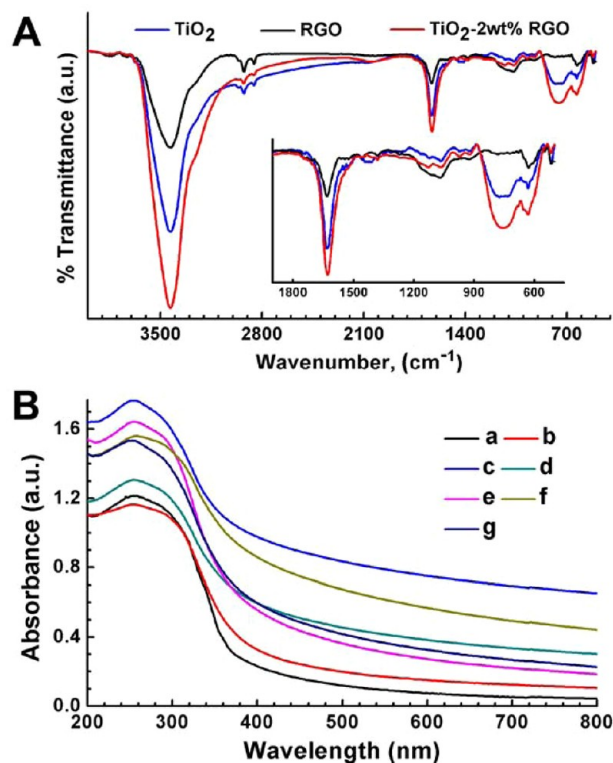

Figure 4. (A) FTIR characterization of TiO$_2$, RGO, and TiO$_2$–RGO nanocomposites. (B) UV–visible absorption spectra of (a) p25, (b)TiO$_2$, (c) TiO$_2$–10 wt % RGO, (d) TiO$_2$–8 wt % RGO, (e) TiO$_2$–5 wt % RGO, (f) TiO$_2$–2 wt % RGO, and (g) TiO$_2$–1 wt % RGO.

shows a broad band at around 3400 cm^{-1}, which is due to the O–H stretching frequency from the surface hydroxyl groups. The peak at 1632 cm^{-1} originates from the hydroxyl groups of molecular water.[42] In the spectrum of RGO, the absorption band appearing at 1550 cm^{-1} is ascribed to the skeletal

vibration of RGO sheets, indicative of the formation of RGO during hydrothermal treatment of GO.[45] This peak is also observed in the spectrum of titania–RGO composite. The FTIR spectrum of RGO also shows absorption bands at 1630 and 1746 cm^{-1}, which are attributed to the stretching vibration of C=C and C=O groups of the residual COOH groups of RGO, respectively.[46] Peaks at 2854 and 2921 cm^{-1} in the spectrum of RGO are due to the CH$_2$ stretching vibration. The broad absorption band centered at 3425 cm^{-1} is attributed to the residual OH groups of RGO. All of the characteristic peaks of RGO are present in the TiO$_2$–RGO composite, as shown in the corresponding spectrum. These results imply that GO was not reduced completely to graphene, and was instead mildly reduced to a RGO product, which contains residual oxygen-containing functional groups, such as –OH and –COOH. Therefore, TiO$_2$ can be susceptible to the interactions with these functional groups of RGO in the nanocomposites. However, unlike in Zhang et al., any appreciable difference between the peaks of TiO$_2$ and TiO$_2$–RGO composites below 1000 cm^{-1} has not been observed, indicative of no formation of a Ti–C bond.[22]

To investigate possible change in the band gap of TiO$_2$–RGO composite, the UV–visible absorption spectra of P25, synthesized TiO$_2$, and its composites with RGO were obtained as shown in Figure 4B. The absorption edge of each sample is determined by the extrapolation of the linear part of the plot to the x-axis. At least qualitatively, the TiO$_2$–RGO nanocomposites show a red shift in the absorption edge compared to those of P25 or synthesized titania. A red shift in the absorption edge is further evidenced by the degradation of a colorless dye, benzoic acid by the TiO$_2$–RGO composite (will be discussed later). However, any particular trend or quantitative change in the shift of absorption edges has not been observed or determined. The same observation was reported by Zhang et al.[40] The shift of the absorption edge of the TiO$_2$–RGO composites was possibly ascribed to be due to the interaction between TiO$_2$ and RGO, which is established by XPS analysis as described in what follows.

The chemical composition of the TiO$_2$–RGO nanocomposite is characterized by Raman spectroscopy as depicted in Figure 5. GO shows a Raman shift at 1344 and 1587 cm^{-1} corresponding to the D- and G-bands, respectively.[47,48] After hydrothermal treatment, the positions of these peaks did not change (red). However, in the TiO$_2$–2 wt % RGO composite
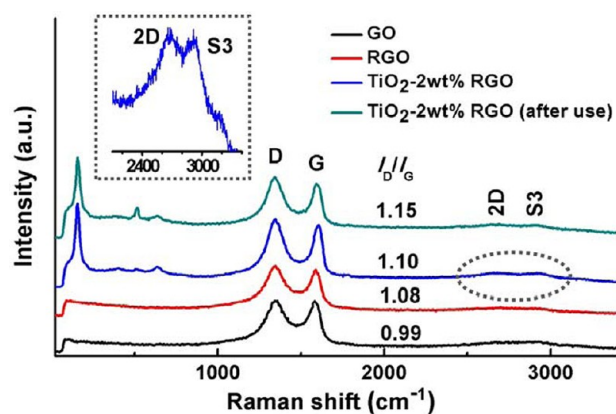

Figure 5. Representative Raman spectra of GO, RGO, and TiO$_2$–RGO.

(blue), the G-band shifted to 1599 cm^{-1} and D-band remained unaltered. The D/G intensity ratio of GO is 0.99; however, this value increases to 1.08 in RGO and 1.10 in TiO$_2$–RGO. The increase in the intensity of D/G ratio indicates a decrease in the average size of the sp^2 domains formed during a hydrothermal reaction. This can be allowed only when newly formed graphitic domains are smaller in size, while more in number as compared to those present in GO before hydrothermal treatment, as reported by Ruoff et al. (see Supporting Information 1 for crystallite size calculation).[49] Apparently, the reduction of GO to RGO is visualized by the color change of the product, in which the brownish reactant turns black. The Raman spectra of TiO$_2$–RGO further shows the presence of peaks at 158, 210, 408, 513 cm^{-1} for E_g, E_g, B_{1g}, and A_{1g}, respectively, for the anatase phase, whereas, the rutile phase is characterized by the modes B_{1g} and A_{1g} at 158 and 630 cm^{-1}, respectively.[50,51] The green line in Figure 5 shows the Raman spectrum of the catalyst TiO$_2$–2 wt % RGO after use. There was almost no change in the D and G-band position as compared to the case before use (blue line). The I_D/I_G ratio of the catalyst after use has an increased value of 1.15 compared to the catalyst before use (1.10). It is attributed to the generation of new carbonaceous defects created by the photocatalytic degradation of the RGO by TiO$_2$ in the composite. Photocatalytic degradation of RGO by TiO$_2$ is discussed in the XPS analysis section.[52] All the samples, especially TiO$_2$–RGO composite shows a symmetric 2D and S3 band. The inset in Figure 5 shows a symmetric 2D-band of TiO$_2$–RGO composite at 2679 cm^{-1}, implying that RGO is present as a single layer graphene in the nanocomposites.[52]

Next, to determine the specific surface area of the porous structured RGO–TiO$_2$ nanocomposites, a nitrogen adsorption–desorption isotherm is measured as depicted in Figure 6.
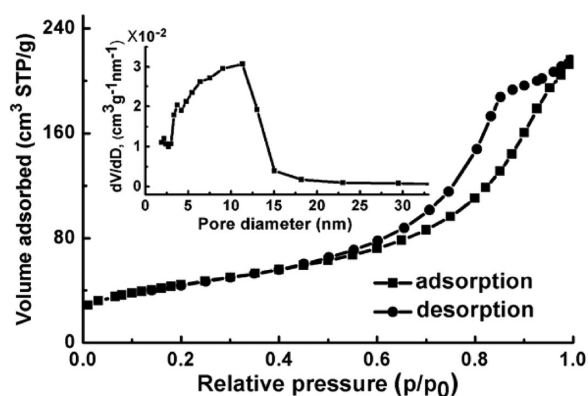

Figure 6. A typical nitrogen adsorption–desorption isotherm of TiO$_2$–RGO nanocomposites. Inset shows typical plot of the pore size distribution.

The isotherm exhibits a type IV with a H1 hysteresis loop according to the IUPAC classification, reflecting the presence of a mesoporous structure of the composites.[53] The synthesized TiO$_2$ shows a larger specific surface area (81.8 m^2/g) than that of P25 (39.0 m^2/g). All of the composites exhibit increased surface areas in accordance with the added amounts of RGO, presumably due to the high theoretical specific surface area (2600 m^2/g) of RGO.[21] The pore-size distribution is also estimated using the Barrett–Joyner–Halenda (BJH) method from the desorption branch of the isotherm. A representative pore-size distribution curve is depicted in the inset of Figure 6,

presenting a peak centered at 11.1 nm. The specific surface area and pore size distribution of different samples are summarized in Table 2.

Table 2. Parameters Obtained from N$_2$ Desorption Isotherm Measurements

samples	^{a}surface area (m^2 g^{-1})	^{b}pore volume (cm^3 g^{-1})	^{c}average pore size (nm)
P25	39.0	0.13	27.9
TiO$_2$	81.8	0.43	15.8
TiO$_2$–1 wt % RGO	99.2	0.26	11.5
TiO$_2$–2 wt % RGO	115.0	0.28	9.3
TiO$_2$–5 wt % RGO	158.7	0.34	7.6
TiO$_2$–8 wt % RGO	169.1	0.20	4.0

^{a}BET specific surface area was calculated from the linear part of the corresponding BET plot. ^{b}BJH desorption cumulative pore volume between 1.7 to 300.0 nm diameter. ^{c}Average pore diameter was estimated from the BJH formula.

To elaborate the chemical states of the elements present in the synthesized TiO$_2$, RGO, and TiO$_2$–RGO composites, XPS characterization is employed, and the spectra are shown in Figure 7. Figure 7A shows the Ti core level XPS spectra of as
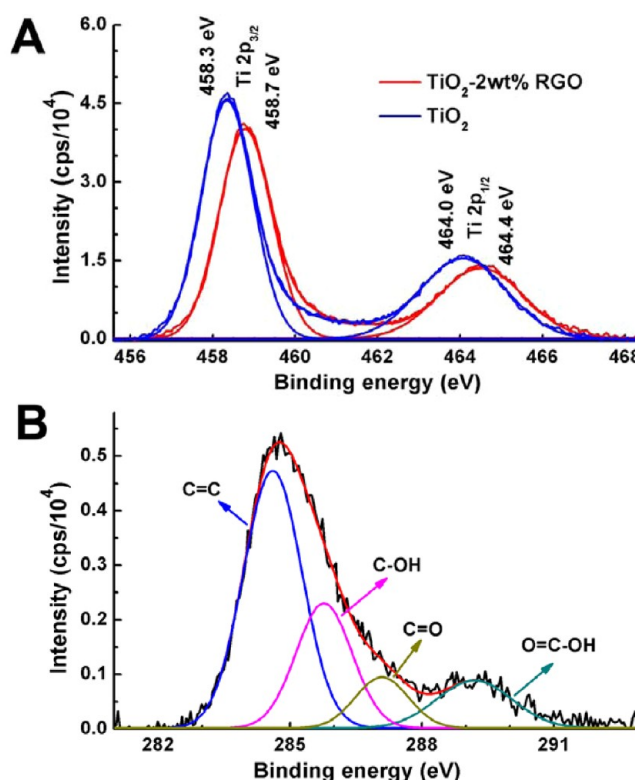

Figure 7. Representative X-ray photoelectron spectroscopy of TiO$_2$–RGO, (A) core level spectra of 2p of TiO$_2$ and TiO$_2$–2 wt % RGO, (B) core level spectra of 1s of C.

synthesized TiO$_2$ and TiO$_2$–5 wt % RGO. The Ti core-level XPS spectrum of TiO$_2$ shows two peaks centered at 464.0 and 458.3 eV, which are assigned respectively to the Ti 2p$_{1/2}$ and Ti 2p$_{3/2}$ spin–orbital splitting photoelectrons in the Ti^{4+} state.[21,52] For TiO$_2$–RGO composite, these two peaks arise at 464.4 and 458.7 eV, respectively.[21,52] In each sample, the splitting between the two Ti-bands is 5.7 eV. These findings imply the

3897

dx.doi.org/10.1021/am301287m | ACS Appl. Mater. Interfaces 2012, 4, 3893–3901

presence of the normal state of Ti^{4+} in the TiO_2 and TiO_2–RGO composites. The difference of 0.4 eV between the Ti peak positions of the as-synthesized TiO_2 and TiO_2–RGO nanocomposite may be attributed to the interactions of Ti with oxygen centers of RGO. As oxygen is a highly electronegative element, it withdraws the electron density from Ti of TiO_2–RGO composites. As a result, the binding energy of Ti in TiO_2–RGO composites increases compared to that of Ti in the as-synthesized TiO_2.[54] To investigate the carbon states in the composites, C 1s core levels are measured, as shown in Figure 7B. Deconvolution of the C 1s peak shows the presence of four different peaks. The peak centered at the binding energy at 284.6 eV is assigned to the presence of C−C, C=C, and C−H bonds of sp^2 carbon of RGO. The peaks at the binding energies 285.7, 287.1, and 289.0 eV are due to the presence of C−OH, C=O, and HO−C=O. However, we did not observe any peak corresponding to the Ti−C bond at ∼282 eV (C 1s) or at 466.0 and 460.3 eV for Ti $2p_{1/2}$ and Ti $2p_{3/2}$, respectively, suggesting no carbon doping in the lattice of TiO_2.[55] However, Akhavan et al. observed the formation of the Ti−C bond in TiO_2–graphene oxide after postannealing at 400 °C.[21] No formation of Ti−C bond in the present system is possibly due to the relatively lower synthetic temperature.

C 1s core level XPS spectra of GO, RGO, and the best photocatalyst, TiO_2−2 wt % RGO, after photocatalytic degradation of RhB were depicted in the Supporting Information 2. Comparison of the area of oxygenated peak ($A_{C−O}$) against graphitic peak ($A_{C−C}$) gives relative elemental compositions of the samples. Table 3 shows the peak area ratio

Table 3. Peak Area Ratio of the Oxygenated Carbon to the Non-oxygenated Carbon and the Total Carbon Band to the Ti band Obtained from XPS Analysis

	XPS		Raman
sample	$^{a}A_{C−O}/A_{C−C}$	$^{b}A_{C}/A_{Ti}$	I_D/I_G
GO	1.44		0.99
RGO	0.70		1.08
TiO_2−2 wt % RGO	0.78	0.17	1.10
TiO_2−2 wt % RGO used	0.44	0.13	1.15

^{a}C−O = C−OH + C=O + OCOH. $^{b}A_{c} = A_{C−C} + A_{C−O} + A_{C−OH} + A_{OC−OH}$.

of oxygen-containing carbon to the nonoxygenated graphitic carbon ($A_{C−O}/A_{C−C}$) and the total carbon band to the titanium band (A_{C}/A_{Ti}) obtained from XPS measurements. GO and RGO have $A_{C−O}/A_{C−C}$ ratios 1.44 and 0.70, respectively. Therefore, it is clear that upon hydrothermal treatment over 50% removal of oxygen containing groups occurs from GO. This result is comparable with the TiO_2 photocatalytic reduction of GO, but it is less than the hydrazine reduction.[56,57] However, in the TiO_2–RGO composites, the extent of GO reduction is less ($A_{C−O}/A_{C−C}$ = 0.78) than that in the RGO under the same reaction conditions. The $A_{C−O}/A_{C−C}$ ratio (0.44) for the catalyst after photocatalytic degradation of RhB shows that further reduction of RGO occurs during dye degradation. Simultaneously, it was observed that A_{C}/A_{Ti} ratio decreased from 0.17 to 0.13. This observation suggests that the TiO_2 nanoparticles degrade RGO after further reduction of it.[52] The same observation was proven by the Raman spectroscopy. The reduction followed by photocatalytic degradation of RGO by TiO_2 has also been reported, which is reasonably comparable with our results presented here.[52]

Finally, to evaluate the photocatalytic activity of TiO_2–RGO nanocomposites obtained in this work, a model reaction of RhB is employed for photodegradation experiments under visible light exposure. Prior to photocatalytic experiment, the dye solution with the catalyst was kept in the dark to attain the absorption−desorption equilibrium of the dye with the catalyst. Figure 8A shows the absorption of RhB by different composite
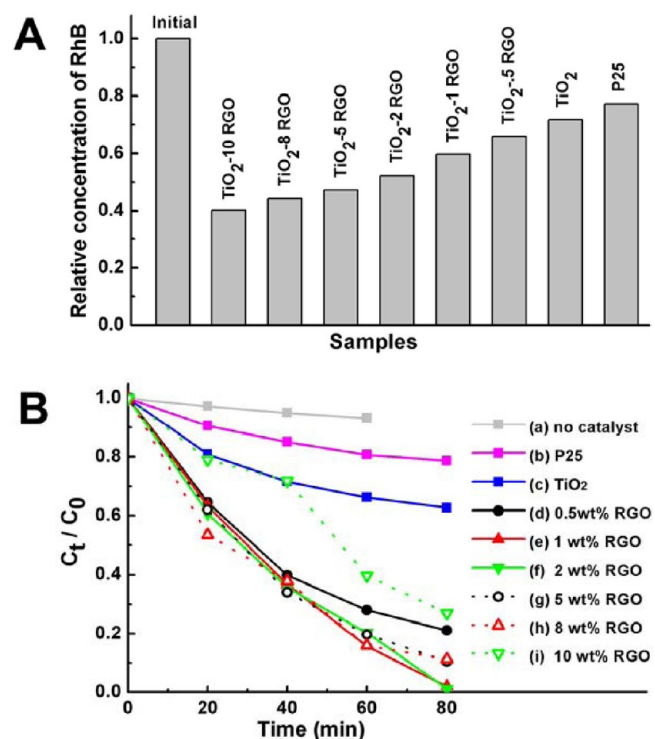

Figure 8. (A) Bar plot showing the remaining relative concentration of RhB after dark absorption by TiO_2–RGO nanocomposites. For comparison, the initial concentration of the dye is indicated. (B) Photodegradation of the RhB dye under visible light irradiation of (a) without catalyst and over the catalyst (b) P25, (c) TiO_2, (d) TiO_2−0.5 wt % RGO, (e) TiO_2−1 wt % RGO, (f) TiO_2−2 wt % RGO, (g) TiO_2−5 wt % RGO, (h) TiO_2−8 wt % RGO, and (i) TiO_2−10 wt % RGO.

catalysts in the dark (see the experimental procedure) as obtained by the UV−visible absorption measurement of the corresponding samples. The result clearly shows that the dye absorption increases with an increase in the amount of RGO in the catalyst, which is associated with the increased surface area of the catalyst as revealed in Table 2. Dye also may be absorbed by π−π interactions between the aromatic region of RGO and the dye molecules.[22]

Figure 8B displays the photodegradation efficiencies of RhB with different catalysts after 80 min of visible light exposure at room temperature and ambient pressure. For comparison, the photocatalytic activity of commercial TiO_2 (P25) is measured under the same reaction conditions. Without the use of a catalyst, the concentration of RhB changes only very slightly (around 6% during 1 h exposure). A similar phenomenon is displayed by RhB in the presence of RGO (not shown). Therefore, RGO does not act as a photocatalyst independently. However, in the presence of a TiO_2–RGO nanocomposite catalyst, photodegradation is remarkably enhanced. The photocatalytic efficiency is maximized at the optimal RGO content in the catalyst. The catalyst with a RGO-concentration

of 2 wt % (TiO$_2$−2 wt % RGO) shows the best catalytic activity. After 80 min, 98.8% of RhB is photocatalytically degraded by the catalyst. Further continuation of the degradation experiment displays almost no absorption peak of RhB at 553.5 nm (For more details, see Figure S2 in the Supporting Information 3 and the explanation therein). The TiO$_2$−1 wt % RGO catalyst shows similar photocatalytic activity. However, below this concentration (e.g., 0.5 wt % of RGO), the catalytic activity is observed to decrease. The same phenomenon was reported by Zhang et al.[40] Notably, all catalysts including the synthesized TiO$_2$ are photocatalytically more active than conventional P25 for the degradation of RhB. This observation is ascribed to the higher surface area (see Table 2) of the synthesized TiO$_2$ and its nanocomposites with RGO compared to P25. The explanation for the RGO-concentration dependence of photocatalytic activity of the nanocomposites is elucidated in the following. In the nanocomposites, dye molecules are adsorbed by both components TiO$_2$ and RGO. As confirmed by the BET surface area measurement, the surface area of the synthesized TiO$_2$ and its nanocomposites with RGO are higher than that of P25. Higher surface area promotes increased dye adsorption (see Figure 8A). At the same time, some active sites of the catalyst (TiO$_2$) are disadvantageously occupied by RGO. This leads to a decrease in the number of the active sites of the catalyst, resulting in reduced photocatalytic activity. These two competing factors are compromised with each other upon 2 wt % loading of RGO, at which the screening of active sites counterbalances the effect of increased surface area. Therefore, the nanocomposite of TiO$_2$−2 wt % RGO shows the best photocatalytic activity. On the other hand, below 1 wt % concentration, the contribution of dye adsorption by RGO may not be sufficiently high as compared to the case of TiO$_2$−1 wt % RGO composite. Therefore, the photocatalytic activity decreases for reduced RGO loading below 1 wt %.

The photodegradation reaction of RhB with the catalysts agrees well with the pseudo-first-order kinetics (considering the first four points). An integrated rate equation is suggested as follows: $\ln(C_0/C_t) = kt$, where C_0 and C_t are the initial concentration and concentration at time t of RhB and k is the apparent degradation rate constant. Rate constants of the degradation reaction for catalysts TiO$_2$, TiO$_2$−0.5 wt % RGO, TiO$_2$−1 wt % RGO, and TiO$_2$−2 wt % RGO are 0.006, 0.021, 0.031, and 0.027 min^{-1}, respectively. In contrast, the rate constant for the commercial TiO$_2$, P25, is 0.003 min^{-1}. Unlike the previously described TiO$_2$-graphene composites, in which only the anatase phase was synthesized, a mixture of both anatase and rutile in our synthesized TiO$_2$ is more active than the P25, which renders an enhanced photocatalytic activity with an order of magnitude difference. Three reasons may account for the enhanced catalytic activity of the TiO$_2$−RGO nanocomposites. First, composites with substantially enhanced specific surface area can provide more active sites and adsorb more reactive species. Second, due to its two-dimensional π-conjugation structure, RGO can act as an electron acceptor, thereby allowing for the photoexcited electrons of TiO$_2$ in the composites to be quickly transferred from the conduction band of TiO$_2$ to RGO. This eventually decreases the rate of recombination of the photogenerated electron−hole pairs, which yields an enhanced photocatalytic activity of the composites.[26] Lastly, the recombination of photogenerated electron−hole pairs can be mitigated *via* accepting electrons by surface hydroxyl groups in both TiO$_2$ and RGO. The

mechanism of dye degradation mainly follows two routes.[22,40,57] The following section is devoted to the studies of the mechanism of dye degradation.

TiO$_2$ can lose oxygen leading to the vacancy formation on the surface as well as in bulk.[58] Oxygen vacancies can also be created in TiO$_2$ because of the doping of other elements such as C, N, or F species to form the partially reduced product of TiO$_{2-\delta}$.[59] In XPS discussion, it was proven that no carbon doping occurred in TiO$_2$. It also excludes the presence of Ti^{3+} and Ti^{2+}. However, since the vacancy formation in TiO$_2$ is a natural phenomenon, it is possible that the concentration of Ti^{3+} and Ti^{2+} is too low to be detected by XPS measurement. Oxygen vacancies can generate some localized states in TiO$_{2-\delta}$ as much as 1.18 eV below its conductance band.[59] To verify this phenomenon, photocatalytic degradation of benzoic acid (BA) was carried out by TiO$_2$−5 wt % RGO under visible light irradiation. BA was chosen as it does not absorb in the visible region (λ_{max} = 227.2 nm). The result was observed by the UV−visible absorption spectra of the reaction mixture at different time intervals during the degradation process (for more details, see Figure S3 in the Supporting Information 4). It is evidently shown that BA was degraded by the catalyst. This experimental observation proves that RhB degradation occurs due to the excitation of TiO$_2$−RGO rather than the photoexcitation of the dye.[22,40,58]

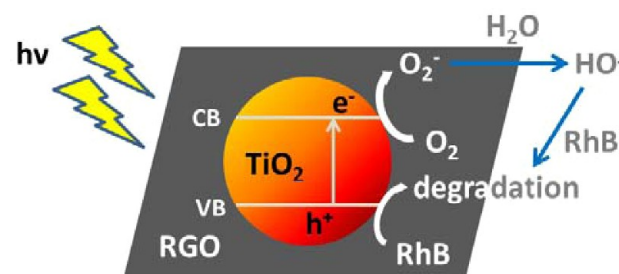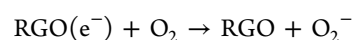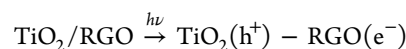Following the above discussion, the proposed mechanism of dye degradation is shown in Figure 9. By the visible light,

Figure 9. Schematic of proposed mechanism of Rhodamine B dye degradation.

valence electrons of TiO$_2$ excited to the conduction band. RGO can act as electron trap and the photogenerated electrons can be transferred to the RGO.[60] The trapped electrons on RGO can react with the dissolved oxygen to form reactive oxygen species.[61] In this way, electron−hole recombination rate decreases. The photogenerated electrons on the TiO$_2$ surface could also be trapped directly by the dissolved oxygen to form reactive oxygen species, which react with water to give hydroxyl radicals. The dye is then degraded by the hydroxyl groups. On the other hand, holes on the valence band of TiO$_2$ react with absorbed water or hydroxyl groups to form surface hydroxyl radicals which then degrade dye. The holes can oxidize the dye molecules directly. The main reactions are shown below.[22,40]

$$\text{TiO}_2/\text{RGO} \xrightarrow{h\nu} \text{TiO}_2(\text{h}^+) - \text{RGO}(\text{e}^-)$$

$$\text{RGO}(\text{e}^-) + \text{O}_2 \rightarrow \text{RGO} + \text{O}_2^-$$

$$\text{TiO}_2(\text{h}^+) + \text{H}_2\text{O}/\text{OH}^- \rightarrow \text{TiO}_2 + \cdot\text{OH}$$

$$\cdot\text{OH} + \text{RhB} \rightarrow \text{degradation products}$$

CONCLUSIONS

TiO_2—RGO nanocomposites are synthesized by a simple and environmentally benign one-step hydrothermal method. TiO_2 is present in both anatase and rutile phases in the nanocomposites. The advantage of this method is that it does not require toxic solvents or chemicals to reduce graphite oxide. However, due to the mild synthesis conditions, graphite oxide is not completely reduced as verified by the FTIR results. Notably, TiO_2—RGO nanocomposites show good photocatalytic activity toward the degradation of RhB dye under irradiation of visible light. The photocatalytic activity increases with decreasing concentrations of RGO in composites. The best catalytic activity is observed with 2 wt % RGO, resulting in RhB degradation of 98.8 wt % after 80 min under visible light. In addition, TiO_2—RGO nanocomposites exhibit an accelerated value ($k = 0.031$ min^{-1}) of the degradation rate constant, which is greater by an order of magnitude than that of P25 ($k = 0.003$ min^{-1}). We anticipate that our green synthetic route to TiO_2—RGO nanocomposites will be beneficially utilized in applications for solar cells and energy storage devices.

ASSOCIATED CONTENT

Ⓢ Supporting Information

Crystallite size calculation; core-level C 1s XPS spectra of GO, RGO, and TiO_2—2 wt % RGO after use; optical images of the reaction mixture at different time intervals during the dye degradation experiment and the corresponding UV–visible absorbance spectra; photodegradation of benzoic acid by the catalyst of TiO_2—5 wt % RGO under visible light with varying irradiation time. This material is available free of charge via the Internet at http://pubs.acs.org.

AUTHOR INFORMATION

Corresponding Author
*Email: pjyoo@skku.edu.
Notes
The authors declare no competing financial interest.

ACKNOWLEDGMENTS

REFERENCES

(1) Alivisatos, A. P. *Science* **1996**, *271*, 933–937.
(2) Kamat, P. V. *J. Phys. Chem. C* **2008**, *112*, 18737–18753.
(3) Zhang, J.; Xu, Q.; Feng, Z.; Li, M.; Li, C. *Angew. Chem., Int. Ed.* **2008**, *47*, 1766–1769.
(4) Ni, M.; Leung, K. H.; Leung, D. Y. C.; Sumathy, K. *Renew. Sust. Energy Rev.* **2007**, *11*, 401–425.
(5) Fujishima, A.; Honda, K. *Nature* **1972**, *238*, 37–38.
(6) Zhou, K.; Zhu, Y.; Yang, X.; Jiang, X.; Li, C. *New J. Chem.* **2011**, *35*, 353–359.
(7) Choi, W. Y.; Termin, A.; Hoffmann, M. R. *J. Phys. Chem.* **1994**, *98*, 13669–13679.
(8) Khan, S. U. M.; Al-Shahry, M.; Ingler, W. B. *Science* **2002**, *297*, 2243–2245.
(9) Chen, X.; Liu, L.; Yu, P. Y.; Mao, S. *Science* **2011**, *331*, 746–750.
(10) Graciani, J.; Alvarez, L. J.; Rodriguez, J. A.; Sanz, J. F. *J. Phys. Chem. C* **2008**, *112*, 2624–2631.
(11) Batzill, M.; Morales, E. H.; Diebold, U. *Phys. Rev. Lett.* **2006**, *96*, 026103.
(12) Rajeshwar, K.; de Tacconi, N. R.; Chenthamarakshan, C. R. *Chem. Mater.* **2001**, *13*, 2765–2782.
(13) Subramanian, V.; Wolf, E. E.; Kamat, P. V. *J. Am. Chem. Soc.* **2004**, *126*, 4943–4950.
(14) Elder, S. H.; Cot, F. M.; Su, Y.; Heald, S. M.; Tyrysgkin, A. M.; Bowman, M. K.; Gao, Y.; Joly, A. G.; Balmer, M. L.; Kolwaite, A. C.; Magrini, K. A.; Blake, D. M. *J. Am. Chem. Soc.* **2000**, *122*, 5138–5146.
(15) Tada, H.; Hattori, A.; Tokihisa, Y.; Imai, K.; Tohge, N.; Ito, S. *J. Phys. Chem. B* **2000**, *104*, 4585–4587.
(16) Tatsuma, T.; Saitoh, S.; Ngaotrakanwiwat, P.; Ohko, Y.; Fujishima, A. *Langmuir* **2002**, *18*, 7777–7779.
(17) Akhavan, O.; Azimirad, R. *Appl. Catal. A: Gen.* **2009**, *369*, 77–82.
(18) Yu, Y. X.; Xu, D. S. *Appl. Catal. B: Environ.* **2007**, *73*, 166–171.
(19) Geim, A. K.; Novoselov, K. S. *Nat. Mater.* **2007**, *6*, 183–191.
(20) Park, S.; Lee, K. S.; Bozoklu, G.; Cai, W.; Nguyen, S. T.; Ruoff, R. S. *ACS Nano* **2008**, *2*, 572–578.
(21) Akhavan, O.; Ghaderi, E. *J. Phys. Chem. C* **2009**, *113*, 20214–20220.
(22) Zhang, H.; Lv, X. J.; Li, Y. M.; Wang, Y.; Li, J. H. *ACS Nano* **2010**, *4*, 380–386.
(23) Kim, H. –il.; Moon, G. –h.; Monllor-Satoca, D.; Park, Y.; Choi, W. *J. Phys. Chem. C* **2012**, *116*, 1535–1543.
(24) Ng, Y. H.; Iwase, A.; Bell, N. J.; Kudo, A.; Amal, R. *Catal. Today* **2011**, *164*, 353–357.
(25) Ng, Y. H.; Lightcap, I. V.; Goodwin, K.; Matsumura, M.; Kamat, P. V. *J. Phys. Chem. Lett.* **2010**, *1*, 2222–2227.
(26) Meng, X.; Geng, D.; Liu, J.; Li, R.; Sun, X. *Nanotechnology* **2011**, *22*, 165602.
(27) Fan, W.; Lai, Q.; Zhang, Q.; Wang, Y. *J. Phys. Chem. C* **2011**, *115*, 10694–10701.
(28) Williams, G.; Seger, B.; Kamat, P. V. *ACS Nano* **2008**, *2*, 1487–1491.
(29) Li, B.; Zhang, X.; Li, X.; Wang, L.; Han, R.; Liu, B.; Zheng, W.; Li, X.; Liu, Y. *Chem. Commun.* **2010**, *46*, 3499–3501.
(30) Zhang, Y.; Pan, C. *J. Mater. Sci.* **2011**, *46*, 2622–2626.
(31) He, Z.; Guai, G.; Liu, J.; Guo, C.; Loo, J. S. C.; Li, C. M.; Tan, T. T. Y. *Nanoscale* **2011**, *3*, 4613–4616.
(32) Wu, B.; Guo, C.; Zheng, N.; Xie, Z.; Stucky, G. D. *J. Am. Chem. Soc.* **2008**, *130*, 17563–17567.
(33) Lambert, T. N.; Chavez, C. A.; Hernandez-Sanchez, B.; Lu, P.; Bell, N. S.; Ambrosini, A.; Friedman, T.; Boyle, T. J.; Wheeler, D. R.; Huber, D. L. *J. Phys. Chem. C* **2009**, *113*, 19812–19823.
(34) Becerril, H. A.; Mao, J.; Liu, Z.; Stoltenberg, R. M.; Bao, Z.; Chen, Y. *ACS Nano* **2008**, *2*, 463–470.
(35) Hummers, W. S.; Offeman, R. E. *J. Am. Chem. Soc.* **1958**, *80*, 1339.
(36) Stankovich, S.; Dikin, D. A.; Piner, R. D.; Kohlhaas, K. A.; Kleinhammes, A.; Jia, Y.; Wu, Y.; Nguyen, S. T.; Ruoff, R. S. *Carbon* **2007**, *45*, 1558–1565.
(37) Kovtyukhova, N. I.; Ollivier, P. J.; Martin, B. R.; Mallouk, T. E.; Chizhik, S. A.; Buzaneva, E. V.; Gorchinskiy, A. D. *Chem. Mater.* **1999**, *11*, 771–778.
(38) Bai, H.; Xu, Y.; Zhao, L.; Li, C.; Shi, G. *Chem. Commun.* **2009**, 1667–1669.
(39) Sher Shah, Md. S. A.; Nag, M.; Kalagara, T.; Singh, S.; Manorama, S. V. *Chem. Mater.* **2008**, *20*, 2455–2460.
(40) Zhang, Y.; Tang, Z. –R.; Fu, X.; Xu, Y. –J. *ACS Nano* **2010**, *4*, 7303–7314.
(41) Park, N.-G.; Schlichthorl, G.; Lagemaat, J.; van de.; Cheong, H. M.; Mascarenhas, A.; Frank, A. J. *J. Phys. Chem. B* **1999**, *103*, 3308–3314.
(42) Hu, Y.; Li, C.; Gu, F.; Zhao, Y. *J. Alloy. Comp.* **2007**, *432*, L5–L9.
(43) Xu, Y. J.; Zhuang, Y. B.; Fu, X. Z. *J. Phys. Chem. C* **2010**, *114*, 2669–2676.
(44) Li, Y.; Li, X.; Li, J.; Yin, J. *Mater. Lett.* **2005**, *59*, 2659–2663.

(45) Nethravathi, C.; Rajamathi, M. *Carbon* **2008**, *46*, 1994−1998.

(46) Park, J. S.; Cho, S. M.; Kim, W. −J.; Park, J.; Yoo, P. J. *ACS Appl. Mater. Interfaces* **2011**, *3*, 360−368.

(47) Kudin, K. N.; Ozbas, B.; Schniepp, H. C.; Prud'homme, R. K.; Aksay, I. A.; Car, R. *Nano Lett.* **2008**, *8*, 36−41.

(48) Ferrari, A. C.; Meyer, J. C.; Scardaci, V.; Casiraghi, C.; Lazzeri, M.; Mauri, F.; Piscanec, S.; Jiang, D.; Novoselov, K. S.; Roth, S.; Geim, A. K. *Phys. Rev. Lett.* **2006**, *97*, 187401.

(49) Stankovich, S.; Dikin, D. A.; Piner, R. D.; Kohlhaas, K. A.; Kleinhammes, A.; Jia, Y.; Wu, Y.; Nguyen, S. T.; Ruoff, R. S. *Carbon* **2007**, *45*, 1558−1565.

(50) Swamy, V.; Muddle, B. C.; Dai, Q. *Appl. Phys. Lett.* **2006**, *89*, 163118.

(51) Choi, H. C.; Jung, Y. M.; Kim, S. B. *Bull. Korean Chem. Soc.* **2004**, *25*, 426−428.

(52) Akhavan, O.; Abdolahad, M.; Esfandiar, A.; Mohatashamifar, M. *J. Phys. Chem. C* **2010**, *114*, 12955−12959.

(53) Sun, L.; Zhao, Z.; Zhou, Y.; Liu, L. *Nanoscale* **2012**, *4*, 613−620.

(54) Dong, F.; Guo, S.; Wang, H.; Li, X.; Wu, Z. *J. Phys. Chem. C* **2011**, *115*, 13285−13292.

(55) Wen, Y.; Ding, H.; Shan, Y. *Nanoscale* **2011**, *3*, 4411−4417.

(56) Shen, J.; Yan, B.; Shi, M.; Ma, H.; Li, N.; Ye, M. *J. Mater. Chem.* **2011**, *21*, 3415−3421.

(57) Bell, N. J.; Ng, Y. H.; Du, A.; Coster, H.; Smith, S. C.; Amal, R. *J. Phys. Chem. C* **2011**, *115*, 6004−6009.

(58) Strunk, J.; Vining, W. C.; Bell, A. T. *J. Phys. Chem. C* **2010**, *114*, 16937−16945.

(59) Zhang, J.; Xiong, Z.; Zhao, X. S. *J. Mater. Chem.* **2011**, *21*, 3634−3640.

(60) Kamat, P. V. *J. Phys. Chem. Lett.* **2011**, *2*, 242−251.

(61) Teoh, W. Y.; Scott, J. A.; Amal, R. *J. Phys. Chem. Lett.* **2012**, *3*, 629−639.